

Outstanding inhibition of H₂O₂ generation in doubly doped graphene: The synergy of two heteroatoms opens a new chemical path

Fernando Aguilar-Galindo^{a,b}, Sergio Fajardo-Rodríguez^{c,d}, José Manuel L. Poyato^c,
Elena Pastor^d, Juan-Ramón Avilés-Moreno^{c,*}, Pilar Ocón^c

^a Departamento de Química, Universidad Autónoma de Madrid, Ciudad Universitaria de Cantoblanco, 28049, Madrid, Spain

^b Institute for Advanced Research in Chemical Sciences (IAdChem), Universidad Autónoma de Madrid, 28049, Madrid, Spain

^c Departamento de Química-Física Aplicada, Universidad Autónoma de Madrid, Ciudad Universitaria de Cantoblanco, 28049, Madrid, Spain

^d Instituto de Materiales y Nanotecnología, Departamento de Química, Universidad de La Laguna, PO Box 456, Santa Cruz de Tenerife, La Laguna, 38200, Spain

ARTICLE INFO

Keywords:

Density functional theory

Doped-graphene

Fuel-cell

Charge transfer

Oxygen reduction reaction

SN enhancement

ABSTRACT

Dual sulfur-nitrogen (SN) doped graphene surfaces have been revealed as a powerful active material in fuel cell applications. The experimental results presented in this work show a clear preference of the material doped with SN towards a 4-electron mechanism, almost completely inhibiting the formation of H₂O₂. However, materials doped only with nitrogen (N) or sulfur (S) favor the 2-electron mechanism, and therefore, the production of H₂O₂. A reasonable theoretical explanation is proposed to justify the inhibition of the H₂O₂ reaction with the use of SN doped graphenes in accordance with the experimental results. The interactions and charge transfer between N and S are the origin of an alternative dissociative step that inhibits the generation of H₂O₂, which is energetically favored, according to Density Functional Theory (DFT) calculations. These two dopant atoms generate a frustrated Lewis pair (FLP), resulting in an enhancement of the catalytic activity of the graphene. Atomic Dipole Corrected Hirshfeld charges (ADCH model) and Non-Covalent Interactions (NCI) are employed to identify the most active sites and support the explanation of the dissociative pathway which inhibits H₂O₂ formation.

1. Introduction

Polymer electrolyte membrane fuel cells (PEMFCs) stand as highly promising devices, proficiently converting chemical energy into electrical power while maintaining low emissions and operational temperatures [1]. The efficiency of an oxygen reduction reaction (ORR), primarily catalyzed by Pt-based noble catalysts in acidic media, plays a pivotal role in the performance of PEMFCs over moderate operating periods. However, the extensive use of platinum (Pt) as a cathodic catalyst presents a substantial impediment due to its cost and the inefficient kinetics associated with ORR [2].

Efforts in recent years have focused on exploring cost-effective alternatives to Pt-based catalysts [3]. Amongst these, N-doped graphenes have emerged as potential candidates, demonstrating comparable efficiency and durability to Pt/C catalysts, due to the electronegativity difference induced by heteroatoms [4–6].

ORR can proceed via both direct 4-electron and 2-electron pathways, yielding hydrogen peroxide as an undesired side product. This,

contributing to the chemical degradation of Nafion® ion exchange membranes commonly used in PEMFCs [7].

In addition to nitrogen-doped graphene catalysts, those incorporating sulfur or phosphorus have also exhibited significant ORR performance [8–11]. Comparative studies have been taken to discern the efficiency of various heteroatom-doped graphene materials [12].

The active centers for this reaction, as proposed in acid media (see section 4.2), are attributed to heteroatoms and adjacent carbons in the graphene structure.

More recently, dual-doped graphenes, such as boron-nitrogen (BN) or sulfur-nitrogen (SN) catalysts, have shown superior ORR performance when compared to their single-element-doped counterparts [13,14]. These studies have explored three fundamental aspects: i) analyzing the state-of-the-art catalysts for the ORR as alternatives to Pt; ii) providing some possible reasons behind the exceptional performance of these materials, particularly the so-called “metal-free” ones; iii) conducting experimental studies, primarily in alkaline media, to validate the efficacy of metal-free catalysts doped with nitrogen and sulfur [15].

* Corresponding author.

E-mail address: juan.aviles@uam.es (J.-R. Avilés-Moreno).

<https://doi.org/10.1016/j.carbon.2023.118499>

Received 7 July 2023; Received in revised form 17 September 2023; Accepted 30 September 2023

Available online 11 October 2023

0008-6223/© 2023 The Authors. Published by Elsevier Ltd. This is an open access article under the CC BY license (<http://creativecommons.org/licenses/by/4.0/>).

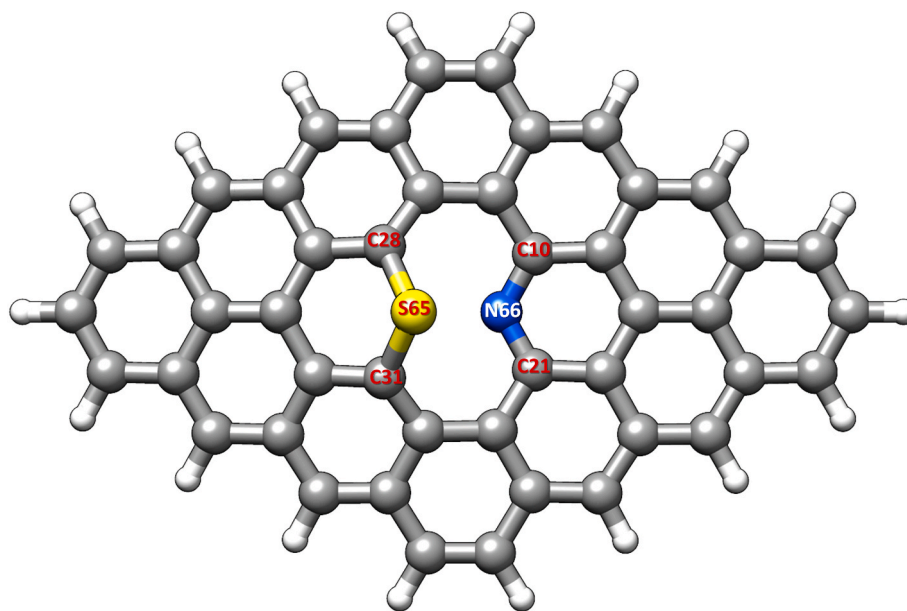


Fig. 1. Optimized geometry of SN-G at the B3LYP/6–31G(d,p) level of theory. Geometrical configuration of heteroatoms and adjacent carbons is showed in the figure. (A colour version of this figure can be viewed online.)

This study focuses on the ORR in acidic media, presenting a novel dissociative step that explains the superior performance of N and S-doped graphene catalysts. The adjacency of these two atoms creates a powerful catalytic system, forming a Frustrated Lewis Pair (FLP) between the lone pair orbital of N and the energetically accessible d orbitals of S, known for their outstanding catalytic properties in homolytic bond breaking [16–18]. For the ORR, the breaking of the O_2 molecule is a critical step; the formation of the OOH intermediate can lead to undesired H_2O_2 production through a 2-electron process. This bidoped catalysts has the potential to dissociate O_2 avoiding the OOH intermediate, thus leading to the 4-electron pathway.

In this work, we demonstrate the remarkable selectivity of SN-doped graphene for the 4-electron process. Our study stands out as one of the few investigations conducted in acidic media concerning the ORR with N and S-based catalysts, yielding exceptional experimental results marked by nearly complete inhibition of H_2O_2 formation in favor of the 4-electron pathway. Through Quantum Chemistry calculations based in the Density Functional Theory (DFT), we analyze reaction mechanisms, including the dissociative step that blocks the undesired peroxide formation, the intermediate structures and free energy values in both; the gas phase and water medium. Our study also includes an explanation of our experimental results through the analysis of ADCH charges and non-covalent interactions (NCI), reinforcing the hypothesis of a strong interaction between S and N atoms that preferentially stabilize the 4-electron pathway.

2. Experimental details

2.1. Synthesis of the catalysts

First, graphene oxide (GO) was synthesized by the Hummers modified method [19] and used as precursor for the synthesis of the catalysts. Non-doped reduced graphene oxide (rGO) was obtained by subjecting GO to thermal treatment within a tubular furnace under a N_2/H_2 (5 % H_2) reduction atmosphere. In contrast, doped-rGO materials were synthesized utilizing a hydrothermal approach. Briefly, a GO dispersion was combined with a reducing agent solution, which also acted as the source of dopants. Specifically, dimethyl sulfoxide (DMSO) was employed for S-rGO, melamine for N-rGO, and thiourea for SN-rGO (see supplementary material for further details).

2.2. Electrochemical characterization

Prior to each measurement, the electrolyte solution was deoxygenated by bubbling Ar into it for 15 min. Then, an activation process was conducted, involving cyclic voltammetry (CV) from -0.4 to 0.8 V vs RHE, at 0.20 V s^{-1} until a reproducible voltammogram was obtained. After, the deoxygenated CV were recorded at 0.01 V s^{-1} . Subsequently, the solution was saturated with O_2 through bubbling for 15 min and CVs were recorded under the same conditions. Moreover, linear sweep voltammetry curves (LSVs) were recorded at 1600 rpm in an O_2 saturated solution in the same potential range as the CVs. The Pt ring potential was fixed at 1.2 V vs RHE during the scans to record the currents caused by the oxidation of the produced H_2O_2 . Both ring and disk currents (I_r and I_d) were registered as a function of the disk electrode potential. Finally, the average number of transferred electrons during the ORR (n) and % of H_2O_2 were calculated.

See supplementary material for a detailed description of the experimental procedures.

3. Computational details

Gaussian 16, Revision C.01 software [20] was used for all the calculations and GaussView 6 [21], Chemcraft [22] and Chimera [23] programs were used for molecular visualizations and analysis. For this task, we selected the well-known B3LYP hybrid functional under the unrestricted formalism [24–29]. In addition, dispersive interactions were calculated using the D2 model of Grimme [26,30].

In this work, the 6–31G(d, p) Pople's double-zeta basis set was selected to optimize the geometry, followed by single-point calculations with the 6–311++G(d,p) basis set to obtain more accurate electronic energies. The surface is described through a surface cluster model, large enough to minimize the border effects of the heteroatoms and adsorbed intermediates (see Fig. 1).

Finally, we have performed an ADCH charges [31] and NCI analysis [32] with Multiwfn software [33] to gain insights into the charge transfer processes. The ORR is simulated in both gas phase and aqueous media. For simulations in aqueous media, the PCM [34] was selected.

See supplementary material for a detailed description of the theoretical procedures.

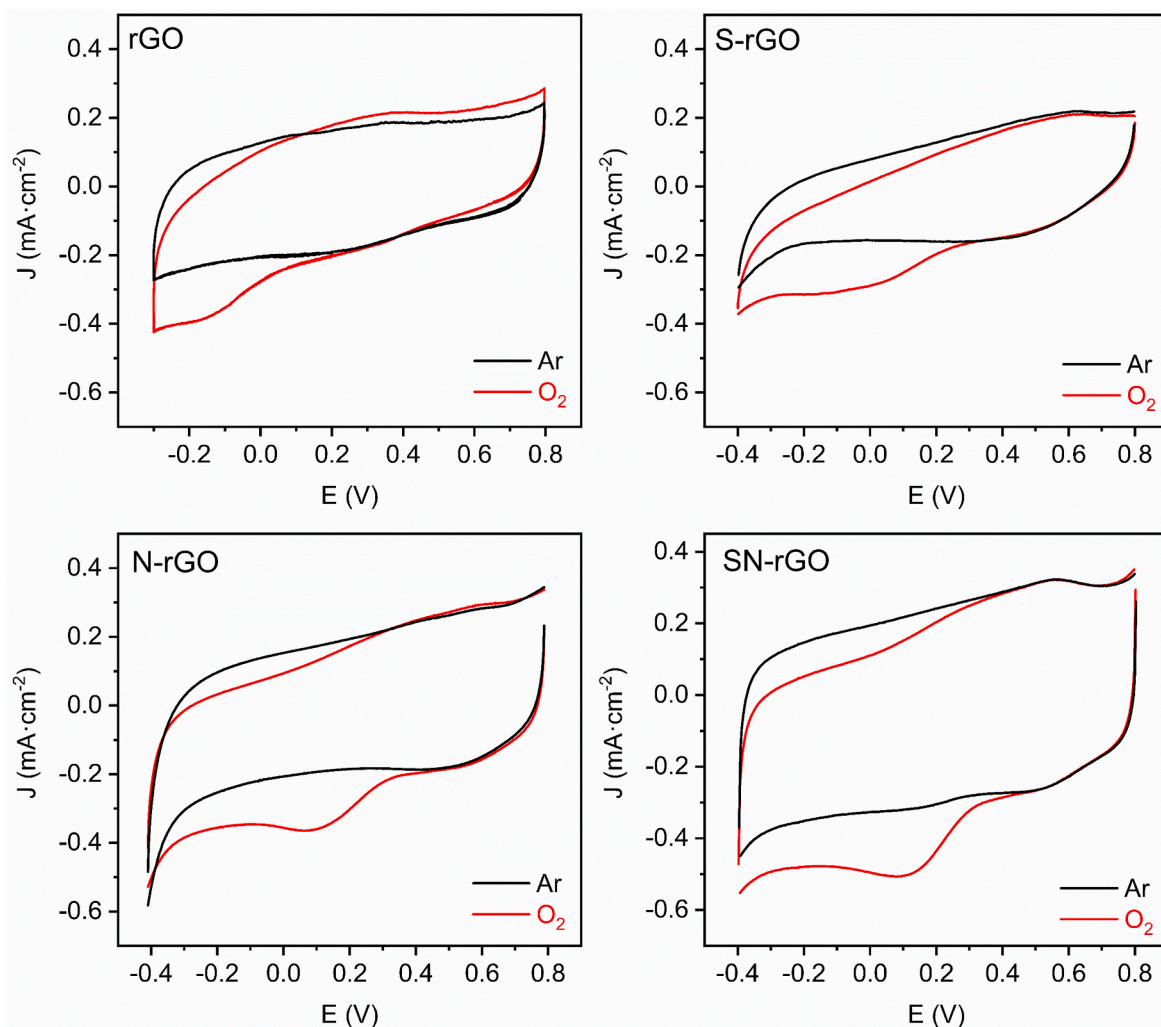


Fig. 2. Cyclic voltammograms recorded in H_2SO_4 0.5 M deoxygenated (black line) and oxygen saturated media (red) at 0.01 V s^{-1} . (A colour version of this figure can be viewed online.)

4. Results and discussion

4.1. Experimental results

4.1.1. Physicochemical characterization

All doped and undoped graphene electrocatalyst were obtained from GO. As expected, throughout the reduced graphene oxide the morphology of the GO is well preserved without noticeable residues of the precursor as shown in scanning electron microscopy (SEM) images (Fig. S1). Note that the incorporation of dopants does not seem to affect the morphology of the sample. According to the Raman results, all catalysts have different concentrations of defects, indicated by different ratios of D-band and the G-band intensity (I_D/I_G). The I_D/I_G values varies between from 0.86 to 1.15, revealing higher defects content for SN-rGO (see Fig. S1) directly correlating with an increased content of active sites [19,35].

X-ray diffraction analyses were conducted on all synthesized catalysts, revealing a distinctive peak at approximately $25^\circ 2\theta$, characteristic of the C(002) diffraction plane of graphite and the vanishing of the 2θ (001) diffraction plane related to the GO. This observation confirmed the successful reduction of [36].

The elemental composition (see Table S2) of the catalyst was determined by elemental analysis, revealing the presence or absence of the N and/or S for the corresponding catalysts and the GO precursor.

In this work, we are describing an active center consisting in a -C-S-C-

group located next to a pyridinic nitrogen, thus, it is important to analyze the nature of the doping atoms in SN-rGO. For this, X-Ray Photoelectron Spectroscopy (XPS) measurements were carried out and described in previous work [35]. XPS analysis revealed that 33% of the nitrogen is in the pyridinic form, while the 85 % of the sulfur atoms are integrated -C-S-C- groups. This substantiates the viability of creating the envisaged N-S environment posited in this study.

4.1.2. Electrochemical characterization

Fig. 2 shows the cyclic voltammogram (CV) of the different materials in deoxygenated solution and oxygen saturated medium. As can be seen in the CVs recorded in deoxygenated solution, only capacitive currents are observed, with slightly higher non-faradaic currents for N-rGO and SN-rGO, which indicates higher surface area or electroactive sites for these doped materials. As reported in previous works [19,35], the more disordered structure of SN-rGO and N-rGO compared to S-rGO can lead to more electroactive sites for the ORR which could explain the higher current densities. A small reversible redox couple can be observed in the potential range 0.3–0.7 V which could be associated to the couple quinone/hydroquinone located on the surface of the materials according to Ref. [37].

When the CVs are recorded in oxygen saturated solution, a cathodic peak associated with the oxygen reduction reaction appears. In the case of rGO and S-rGO, the reduction peak is not well defined and only little faradaic current resulting from oxygen reduction is observable.

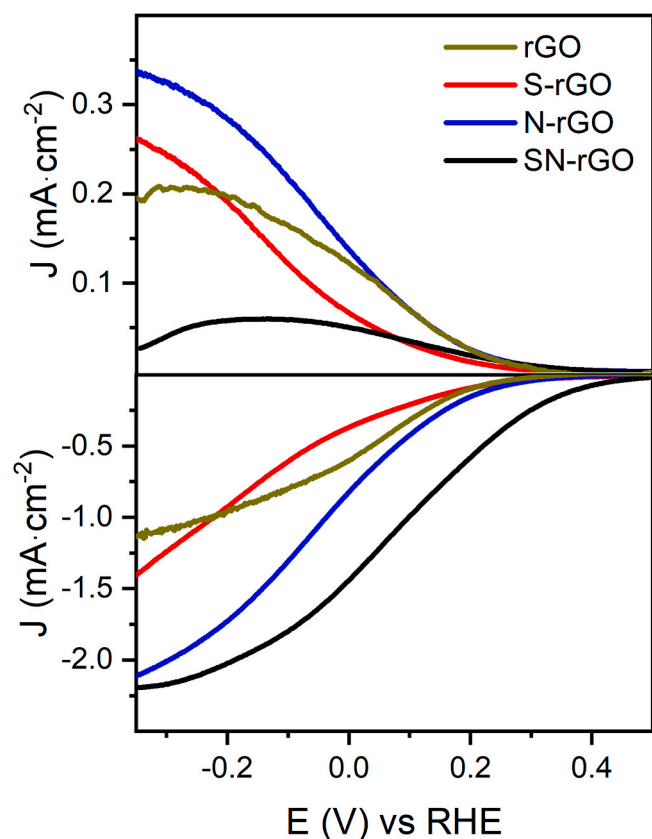


Fig. 3. LSVs recorded at 1600 rpm in H_2SO_4 0.5 M at 2 mV s^{-1} . Ring measures (top) and disk measures (bottom). (A colour version of this figure can be viewed online.)

Furthermore, the onset potential (E_{onset} , defined as the potential at -0.1 mA cm^{-2} , being a negative value since it is a reduction process) of these materials is located at more negative value compared to N-rGO (0.24V) and SN-rGO (0.38V), indicating a more sluggish kinetic for the ORR in the former. SN-rGO also shows a reduction peak potential (E_{peak}) of 0.12 V while the E_{peak} for N-rGO is 0.10 V, thus demonstrating the higher electrocatalytic activity of the dual-doped material. Besides, SN-rGO is the material that develops the highest current densities with -0.50 mA cm^{-2} compared to -0.44 , -0.38 and -0.32 mA cm^{-2} at E_{peak} for N-rGO, rGO and S-rGO, respectively.

4.1.3. Electrocatalytic activity

To evaluate the electrocatalytic activity, linear sweep voltammetry measurements are carried out using a Rotating Ring-Disk Electrode (RRDE). Fig. 3 shows the cathodic (bottom) and anodic (top) current densities corresponding to the oxygen reduction on the disk and H_2O_2 oxidation at the Pt ring to oxygen, respectively. It can be observed that S-rGO develops lower current density values compared with N-rGO and SN-rGO, and even minor than rGO at low overpotentials. The inferior slope value in the mixed control region of the polarization curve suggests a more hindered oxygen reduction. N-rGO and SN-rGO develop similar current densities, nonetheless, SN-rGO is the material with higher E_{onset} , shifted 140 mV to more positive potentials compared to N-rGO, and 190 mV compared to S-rGO. Besides, SN-rGO displays lower anodic currents in the Pt ring, indicating higher electron transfer during the ORR.

The number of electrons (n , eq. S1) and % of H_2O_2 were determined from the RRDE measurements data and plotted as a function of the potential (see Fig. 4). At low overpotentials (0.25–0.4 V vs RHE), S-rGO values are close to $3.5 e^-$, indicating that the ORR occurs mainly via the

$4 e^-$ pathway. However, as the overpotential increases, a decrease in the value of n is observed with values below $3 e^-$, which indicates a competition between the mechanism of the 4 and the 2 electrons with predominance of the reduction of oxygen to H_2O_2 . In the case of N-rGO, in the low overpotential region the n values are close to $2.5 e^-$ and rapidly increase to $2.75 e^-$, showing a constant behavior in the whole potential window. Lastly, SN-rGO present values between 3.7 and $3.8 e^-$ indicating that the ORR proceeds mainly by the $4 e^-$ electron pathways. These trends are also corroborated from the results obtained with the Pt ring, where the H_2O_2 produced during the ORR at the disk electrode is collected and detected at the ring electrode by H_2O_2 electrooxidation to O_2 . The % of H_2O_2 obtained is included in Fig. 4 finding that the percentage of intermediate H_2O_2 produced during ORR and determined using eq. (S2), confirms that the lowest amount is obtained by the SN-rGO catalyst.

There are several works describing the catalytic activity of doped graphene-based materials towards the ORR (see Table 1). Jiajie et al. unveiled the effect of N, S doping in graphene to explore its ORR activity, finding that the maximum n value obtained was 3.9 at 0.6 V vs RHE [38]. Similarly, You et al. [39] found that the number of electrons transferred during the ORR varies in the range of 3.4 – $3.9 e^-$. They also compared the dual-doped material with a N-rGO, revealing that for this material the ORR proceeds mainly by the 2 electrons pathway with a maximum n value of 3.3 at which is in accordance with our work. In alignment with our study, S. Bag et al. [40] conducted a comparative assessment of the electrocatalytic performance of N, S, and NS-rGO materials in an alkaline environment, yielding findings akin to those of our investigation. Their findings suggested that the simultaneous integration of N and S into the rGO framework led to a notable reduction in the production of HO_2^- , affirming the synergistic effect between these heteroatoms.

Nevertheless, despite the plethora of research focused on elucidating the catalytic activity of nitrogen and sulfur dual-doped rGO for the ORR in alkaline environments, the availability of experimental investigations addressing similar behaviour under acidic conditions remains noticeably limited.

Mass-transport corrected Tafel plots, E vs J_k , are obtained from LSV data and shown in Fig. 5. The J_k is the net kinetic current density, obtained from the experimental current density J by the following equation (1)

$$J_k = \frac{J \cdot J_L}{J_L - J} \quad (1)$$

Where $\frac{J_L}{J_L - J}$ is the diffusion contribution correction and J_L is the limiting diffusion current density. It is important to highlight that the limiting current used for the mass-transport correction is not well defined, especially for S-rGO, thus, it was chosen the current at -0.3 V as the limiting current. From the Tafel plots it is possible to determine some parameters that allows to identify the nature of the ORR at the different materials. First, a change in the Tafel slope is associated to a change in the mechanism of the reaction. In the case of rGO, N-rGO and SN-rGO, two different Tafel slopes can be distinguished at low and high overpotentials, indicating a potential dependent mechanism for the ORR in these materials. Nonetheless, only one Tafel slope is close to 60 mV dec^{-1} can be fitted for S-rGO, N-rGO and SN-rGO at low overpotential and indicates that the rate determining step (RDS) is the first electron transfer under Temkin adsorption conditions for the surface intermediates O-containing or a chemical step as RDS following the primary electron transfer. In the case of rGO at low overpotentials, a 90 mV dec^{-1} slope is observed, which would probably be the result of a competition of at least two electrochemical processes as a rate determining step, or the adsorption of H_2O_2 species on the surface of the electrode during the ORR, blocking electroactive sites of the catalyst.

At higher overpotentials, SN-rGO develops a slope close to 120 mV dec^{-1} , which could indicate a change in the mechanism from

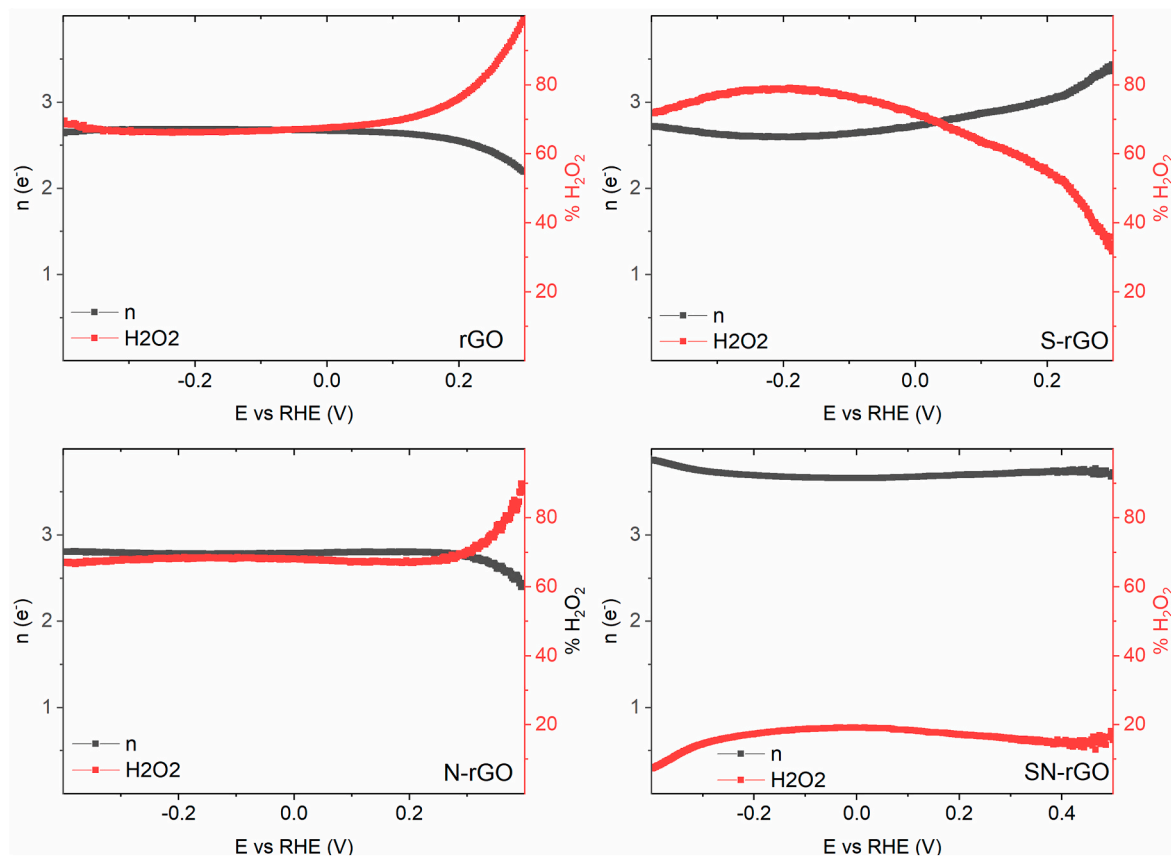


Fig. 4. Number of electrons (n) transferred during the ORR (black) and the % of H_2O_2 (red) produced as function of the potential applied. (A colour version of this figure can be viewed online.)

Table 1

Comparison of number of electrons transferred during the ORR with different works.

Material	n (e^-)	H_2O_2 (%)	Electrolyte	REF.
SN-rGO	3.8	18	H_2SO_4 0.5 M	This work
SN-rGO	3.8	16	KOH 0.1 M	[41]
S-rGO	2.5	72	KOH 0.1 M	[42]
SN-rGO	3.2–3.9	12	KOH 0.1 M	[40]
SN-rGO	3.5–3.7	16–28	KOH 0.1 M	[43]
N-rGO	3.1	40	KOH 0.1 M	[40]
S-rGO	2.9	55	KOH 0.1 M	[40]

Temkin to Langmuir adsorption and the first electron transfer as the RDS [44]. In the case of rGO and N-rGO, the obtained slopes at high overpotentials exceeds $120 \text{ mV} \cdot \text{dec}^{-1}$ (see Table 2). This can be explained by the higher H_2O_2 production, which is adsorbed on the surface of the graphene material producing a blockage effect of the active sites that increase the Tafel slope (see Fig. 5) [45]. This effect can also be considered for S-rGO for which the ORR proceeds by a mixture of the $2e^-$ and $4e^-$ pathways (see Fig. 4). However, as seen in previous works [35], S-rGO is the material with higher oxygenated functional groups (OFGs) on the surface, that could also produce a blockage effect of the active sites since the OFGs inhibit the adsorption of oxygen. This may explain the higher Tafel slope associated to a more hindered ORR process [45,46].

From the intercept of the linear portion of the Tafel analysis it is possible to calculate the exchange current density (j_0), defined as the magnitude of the current at equilibrium potential, and which is widely used for evaluating the catalytic properties of a catalyst (see Table 2) [47,48]. S-rGO and rGO are the materials with lower j_0 indicating a

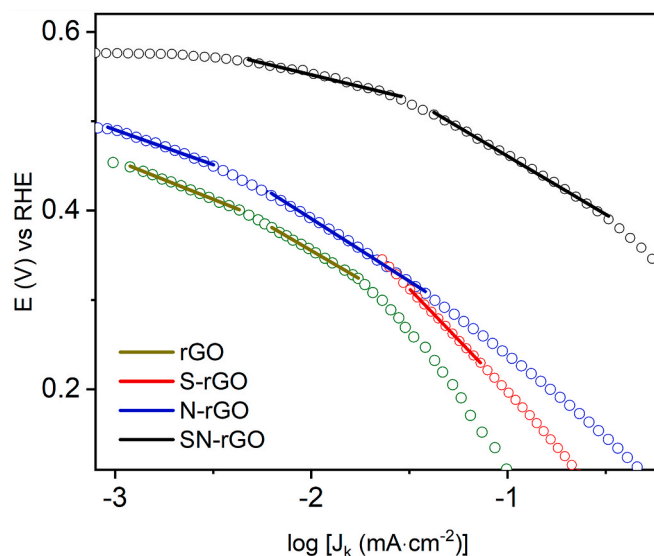


Fig. 5. Mass-transport corrected Tafel plots of the different catalyst. rGO (green), S-rGO (red), N-rGO (blue) and SN-rGO (Black). (A colour version of this figure can be viewed online.)

more hindered ORR. N-rGO shows better performance with a j_0 of $3.4 \cdot 10^{-16} \text{ A cm}^{-2}$ which is one order of magnitude higher than those of S-rGO and rGO. Lastly, SN-rGO develops greater j_0 values, with three orders of magnitudes upper than N-rGO at low overpotentials and 2 orders higher at more positive overpotentials (see Table 2). This result demonstrates the effectiveness of the SN-rGO as a catalyst for the ORR.

Table 2

Different parameters obtained from LSV measurements and Tafel plot (o.p. denotes overpotentials).

Material	E_{onset} (V) ^a	Tafel slope (mV dec ⁻¹)		j_0 (A·cm ⁻²)	
		low o.p.	high o.p.	j_0 low o.p.	j_0 high o.p.
rGO	0.20	90	137	$2.1 \cdot 10^{-17}$	$7.5 \cdot 10^{-11}$
S-rGO	0.19	228	–	$1.1 \cdot 10^{-17}$	–
N-rGO	0.24	77	143	$3.4 \cdot 10^{-16}$	$8.7 \cdot 10^{-9}$
SN-rGO	0.38	61	130	$9.9 \cdot 10^{-13}$	$1.2 \cdot 10^{-7}$

^a The E_{onset} is defined as the potential that corresponds to -0.1 mA cm^{-2} .

Table 3

Relative energies (eV) of the first steps calculated with the inclusion of weak interactions through D2 and D3BJ schemes with respect to the reactants (O_2 and graphene).

	D2	D3BJ
Physisorption	0.30	0.32
Non-dissociative chemisorption	2.01	1.97
Dissociative chemisorption	-1.36	-1.41

While these results partly account for the enhanced cathodic currents observed in SN-rGO, they fall short of explaining the exceptional H_2O_2 inhibition observed. To delve deeper into the underlying mechanism of the oxygen reduction reaction (ORR), we turned to DFT calculations. By employing computational calculations, DFT offers novel insights into the intricate details of the ORR mechanism, shedding light on the reasons behind the remarkable performance of SN-rGO in acidic environments.

4.2. Theoretical results

4.2.1. Reaction mechanisms

Based on the experimental results, it seems that the only material that completely (or almost) inhibits the 2-electron mechanism is SN-doped graphene. For this reason, this material has been selected as the main target of the theoretical study to better understand its behavior.

The ORR reaction was modeled on a doped graphene surface as shown in Fig. 1. This model has been used successfully in previous works [12]. Given the size of the sheet, ($\text{C}_{46}\text{SNH}_{18}$), where dopant atoms are far from the edges, the border effects can be minimized, and a more realistic situation of the catalyst action is performed. Other studies [49, 50] have predicted that the most stable substitution of S and N in a graphene layer is in adjacent position. In this way, we have used that configuration to model the 2- and 4-electron pathways.

The inclusion of an atom of the third period of the periodic table (such as S) results in structures with a local distortion of the graphene layer and the S atom being out-of-plane, which has important implications in the most favored mechanism.

Table 4

Reaction free energies for each step of the ORR, dissociative pathway, in the SN-doped graphene model for a four-electron transfer mechanism in the gas phase and water (PCM) phase.

Dissociative pathway ^a		
ORR free energies/eV	SN-G Gas	SN-G Water
Step 1	-1.07	-1.36
Step 2	-9.38	-6.19
Step 3	-10.11	-7.46
Step 4	-9.54	-5.84
Step 5	-10.10	-7.33
Total	-40.20	-28.19

^a Energies for non-dissociative pathway are shown in Table S3 of supplementary material. B3LYP/6-311++G(d,p)/B3LYP/6-31G(d,p) level of theory with D2 dispersion model.

In this study, we focused on a neutral charge system compounded by the SN-rGO and the oxygen molecule, where the first reaction step corresponds to the simulation of O_2 adsorption on the SN-doped. To simulate the subsequent reaction steps of the ORR, an additional proton (defined as $\text{H}_3\text{O}^+ - \text{H}_2\text{O}$, to consider in an adequate way the proton affinity) and one extra electron were introduced in each step. Equilibrium geometries of these species were obtained at each stage, allowing us to construct the energy profile of the ORR.

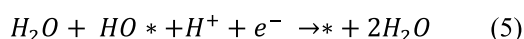
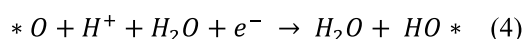
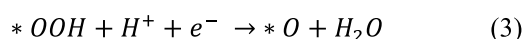
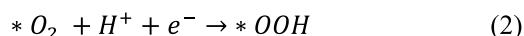
The ADCH and NCI charge analysis results indicates that the heteroatom and the carbon atoms directly bonded to the heteroatom exhibit the most promising characteristics for acting as active sites.

We have selected the D2 model to compare the results of this work with those obtained in our latest study of monodoped graphenes [12]. In order to assure the good performance of D2 model, we computed the first steps (physisorption, non-dissociative chemisorption and dissociative chemisorption) using the D3 correction with the Becke-Johnson damping (D3BJ), being the energy difference of the order of 0.05 eV or lower ($\sim 1 \text{ kcal/mol}$, below the accuracy of DFT). Comparison of the performance of two methods for the first steps, which determine the chemical path, is shown in Table 3.

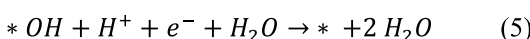
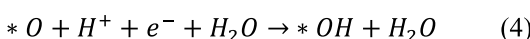
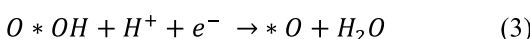
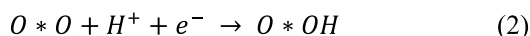
Furthermore, the chemical environment in which heteroatoms are located, is very important for catalytic activity of the ORR. Previous XPS analysis shows that 35 % of the N present in the SN-rGO dual-doped catalyst is in the pyridinic form [35]. It is known that the pyridinic form of N is more active for ORR and therefore a 4-electron mechanism follows. In our work, the design of the catalyst has been based on previous studies [12,49] that concluded that both heteroatoms (N and S) are found in a pyridine-like environment. In this way, the design of our dual-doped catalyst takes these aspects into account and we have built a dual-doped graphene where the active center is S, enhanced precisely by the chemical environment and, especially, by the interaction with N.

In previous studies [12,49] the mechanism shown in Scheme 1 has been proposed. However, along the reaction mechanism, the OOH intermediate, produced in the second step of the non-dissociative

Non-dissociative pathway



Dissociative pathway

**Scheme 1.** Non dissociative and dissociative pathways of the oxygen reduction reaction.

Marked in red, dissociative and non-dissociative adsorptions of O_2 ; * denotes the active site(s) of the doped graphene.

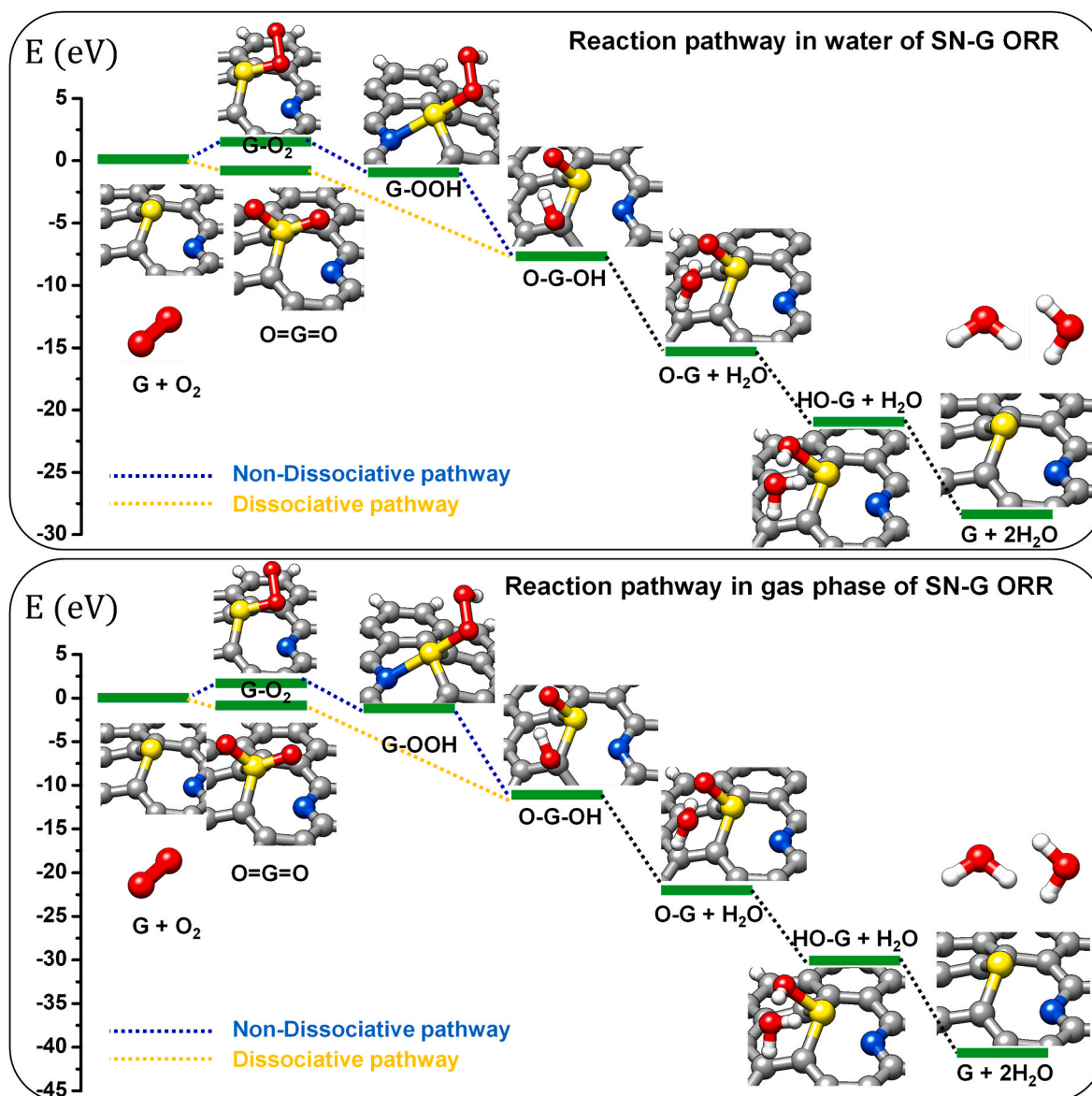


Fig. 6. Optimized geometries for the proposed dissociative (orange) and non-dissociative (blue) mechanisms for ORR with SN-doped graphene in solution (water, upper figure) and gas (lower) phases. Colour labels: C: grey, N: blue, O: red, Sulfur: yellow, H: White. (A colour version of this figure can be viewed online.)

mechanism, can evolve via a two-electron mechanism towards H_2O_2 instead to 2OH , leading to the formation of hydrogen peroxide. This is an undesired side reaction, since it inhibits the formation of the final product (water) and it is also a very reactive specie that can damage the electrode.

To avoid the generation of H_2O_2 , the perfect catalyst should prevent the formation of the intermediate OOH adsorbate. In this way, the breaking of the O–O bond prior to the first reduction through dissociative adsorption is desired. For the dual SN-doped graphene, we found that this dissociative adsorption is energetically favored (see Table 4, Figs. S2 and S3), thus avoiding the formation of H_2O_2 and promoting the desired reaction pathway for the 4-electron mechanism, in excellent agreement with experimental measurements as discussed in the experimental section. The energy barrier of this step is small ($\Delta G^\ddagger = 0.6$ eV with respect to the non-dissociative O_2 chemisorption), and thus it is energetically accessible at the experimental conditions [51]. In line with a previous study [12] a four-electron transfer mechanism is assumed, denoting the surface as *. Consequently, the complete mechanism for this catalyst is as follows.

The pathways shown in Scheme 1 address the non-dissociative and

dissociative mechanisms as follow: i) first a O_2 molecule is placed close to the doped surface and the geometry of the system is optimized. This is the decisive step to prevent the formation of H_2O_2 . If chemisorption is non-dissociative, step 2 may form OOH, an essential precursor for the 2-electron mechanism. However, dissociative chemisorption prevents the formation of this precursor and ensures a 4-electron mechanism; ii) the following four steps are properly the reduction reactions that involve a total of 4 protons and 4 electrons to obtain water as the main product, except in the non-dissociative mechanism that will form the OOH precursor that may also evolve by a 2-electron mechanism. The energy difference between product and reactants is the reaction energy. The resultant reaction free energies are given in Tables 4 and S3.

Optimized geometries of the reaction products for the whole mechanisms (dissociative and non-dissociative) were analyzed and are shown in Fig. 6. As can be seen, the bond formation between the surface and the OOH species takes place on the heteroatom. Steps 1 and 2 of the non-dissociative mechanism involve the formation of the *OOH intermediate, which allows the 2-electron mechanism and, therefore, the formation of H_2O_2 . However, the new proposed mechanism involves a first dissociative chemisorption of the O_2 molecule, inhibiting the formation

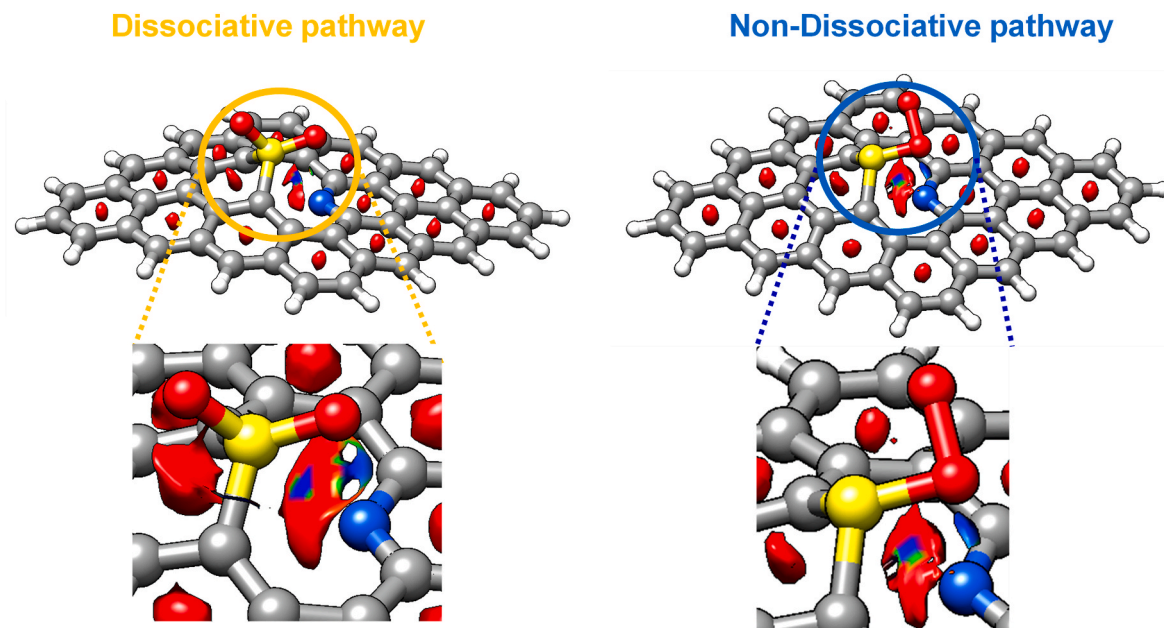


Fig. 7. Non-covalent interaction (NCI) analysis of the dissociative (left) and non-dissociative (right) chemisorption of O₂. Contributions from dispersive attractions (green color), along with hydrogen bonding and strong attractions (blue color) and weak steric repulsive interactions (red color) are shown. (A colour version of this figure can be viewed online.)

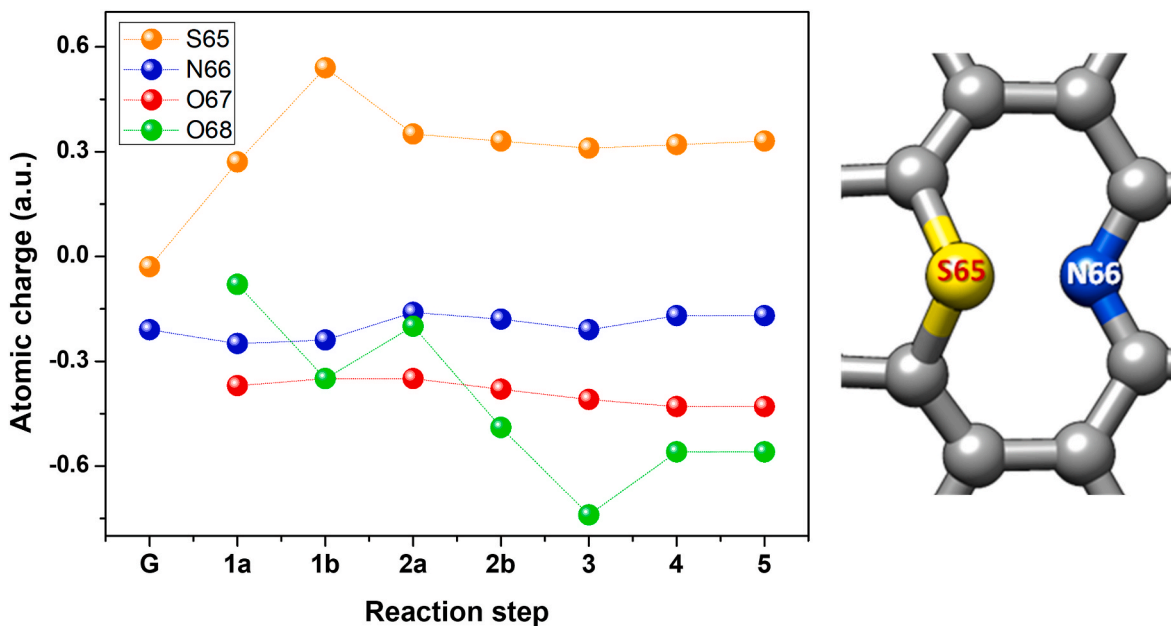


Fig. 8. Charge evolution (atomic units) on the active centers in the SN doped surface along the different steps. 1a and 1b refer to non-dissociative and dissociative adsorption. O67 and O68 are included for direct inspection. 1a and 2a: non-dissociative steps; 1b and 2b: dissociative steps. (A colour version of this figure can be viewed online.)

of the *OOH intermediate, and a subsequent H^+e^- reaction to form the O*OH intermediate that will follow a 4-electron mechanism. The next steps of both mechanisms involve a series of H^+e^- reactions to release 2H₂O molecules. In comparison with our last work [12], the general results differ significantly from those previously reported by us using different dopants.

4.2.2. Analysis of the electron density

Non-covalent interaction (NCI) analysis was used to enhance the visualization of the interactions occurring during the four-electron pathway. This offers a chemically intuitive representation of electronic

interactions through the utilization of iso-surfaces derived from electron density gradient [32]. Additionally, by examining the sign of the second Hessian eigenvalue of the electron density, it becomes possible to distinguish between various types of non-covalent interactions. Fig. 7 illustrates the results of the NCI analysis of the most conformers of the dissociative and non-dissociative chemisorption of the O₂. Fig. S4 shows the NCI plot of each step of the four-electron mechanism. Separate contributions from strong interactions as hydrogen bonds (blue color), weak non-covalent interactions as dispersive attractions (green color), and steric repulsive congestion (red color) are shown.

The NCI analysis confirms a greater stabilization of dissociative O₂

chemisorption compared to non-dissociative homolog (see Fig. 7). In both cases there is a strong S–N interaction marked in blue which stabilizes the structure. In addition, in the dissociative adsorption there is a strong interaction between one of the oxygens and the N atom, being this situation more stable than the non-dissociative adsorption case. This fact is in good agreement with the experiments since the dissociative mechanism inhibits the formation of H₂O₂.

In order to better understand the charge transfer effects that could exist between N and S, we have studied the evolution of charges (ADCH model) in each step of the mechanism. Fig. 8 summarizes the analysis presented in this work. It is very interesting to see how during the physisorption stage, the N and S charges remain constant and with negative values, −0.2 and −0.05 in atomic units, respectively, having nitrogen a more negative value as expected. We also observe how N maintains its charge practically constant during all steps. However, S undergoes a very pronounced charge transfer process during the non-dissociative and dissociative chemisorption stages, being the last the largest change for S. In fact, during the dissociative stage, S increases its charge to +0.5, more than twice that the value obtained during the non-dissociative step. This fact is very relevant and confirms the results obtained by NCI and experimentally. This dissociative step is especially stable, and one of the reasons could be this intense N–S interaction, in addition to the O–S interaction that strongly stabilize this stage.

5. Conclusions

We would like to highlight that the novelty of our work is twofold: i) first, from an experimental point of view, it is one of the scarce works in the bibliography that studies ORR in an acid medium and with a dual-doped catalyst that shows such impressive results for the 4-electron pathway; ii) second, from the theoretical point of view, we provide an exhaustive study of the different reaction steps, showing for the first time, a new dissociative steps that agrees well with the inhibition of H₂O₂ formation and favors the mechanism of 4 electrons.

This study has successfully demonstrated that the electrocatalytic activity of reduced graphene oxide materials for the oxygen reduction reaction can be significantly influenced by the incorporation of heteroatoms such as N and S into the graphene structure. Tafel analysis indicates a potential-dependent mechanism for the ORR in these graphene-based catalysts. Through cyclic and linear sweep voltammetry using a rotating ring-disk electrode, it has been observed that SN-rGO exhibits superior performance against ORR compared to the other catalysts. This enhanced performance can be attributed to a new dissociative chemisorption step of O₂ facilitated by the N and S interaction in the graphene structure. The experimental results consistently support the involvement of this new step, which effectively suppresses the formation of H₂O₂ and favors the 4-electron mechanism.

The new dissociative step is more energetically favorable compared to non-dissociative chemisorption. The NCI analysis points to a strong O, N and S interaction at this step, which stabilizes the structure against the non-dissociative step. In addition, a study of the evolution of the electron density confirms this fact since a strong transfer of charge between O and S occurs, which reinforces the interaction between S and N. The key point of the efficiency of this substrate as ORR catalyst is the labile nature of the S–N interaction, which allows for a rich chemical reactivity of the sulfur atom.

We believe that the symbiosis of experimental work with theoretical analysis it is critical for smarter design of the most efficient catalysts for ORR.

CRediT authorship contribution statement

Fernando Aguilar-Galindo: Conceptualization, Methodology, Software, Validation, Formal analysis, Investigation, Resources, Data curation, Writing – original draft, Writing – review & editing, Visualization. **Sergio Fajardo-Rodríguez:** Conceptualization, Methodology,

Software, Validation, Formal analysis, Investigation, Resources, Data curation, Writing – original draft, Writing – review & editing, Visualization. **José Manuel L. Poyato:** Formal analysis, Methodology, Resources, Writing – review & editing, Supervision. **Elena Pastor:** Formal analysis, Methodology, Resources, Writing – review & editing, Supervision. **Juan-Ramón Avilés-Moreno:** Formal analysis, Methodology, Resources, Writing – review & editing, Supervision. **Pilar Ocón:** Formal analysis, Resources, Writing – review & editing, Supervision, Project administration, Funding acquisition, All authors have read and agreed to the published version of the manuscript.

Declaration of competing interest

The authors declare that they have no known competing financial interests or personal relationships that could have appeared to influence the work reported in this paper.

Acknowledgments

This work was supported by the Madrid Regional Research Council (CAM) and ERDF (European Regional Development Fund), grant n. P2018/EMT-4344 BIOTRES-CM. We thank the Spanish Ministry of Economy, PID2020-116712RBC21, PID2020-117586RB-I00, PID2022-138470NB-I00 and PID2019-110091 GB-I00 projects funded by MCIN/AEI/10.13039/501100011033. S. Fajardo acknowledge the MCIN for the pre-doctoral grant (PRE2018-085718). We also thank the CCC UAM (Graforr project) for allocation of computer time. We acknowledge Dr. F. Gamez (Complutense University of Madrid) for extensive English corrections.

Appendix A. Supplementary data

Supplementary data to this article can be found online at <https://doi.org/10.1016/j.carbon.2023.118499>.

References

- [1] A. Rabis, P. Rodríguez, T.J. Schmidt, Electrocatalysis for polymer electrolyte fuel cells: recent achievements and future challenges, *ACS Catal.* 2 (5) (2012) 864–890, <https://doi.org/10.1021/cs3000864>, may.
- [2] H. Cruz-Martínez, H. Rojas-Chávez, P.T. Matadamas-Ortiz, J.C. Ortiz-Herrera, E. López-Chávez, O. Solorza-Feria, D.I. Medina, Current progress of Pt-based ORR electrocatalysts for PEMFCs: an integrated view combining theory and experiment, *Mater. Today Phys.* 19 (2021), 100406, <https://doi.org/10.1016/j.mtphys.2021.100406> jul.
- [3] L. Lai, J.R. Potts, D. Zhan, L. Wang, C. Kok Poh, C. Tang, H. Gong, Z. Shen, J. Lin, R. S. Ruoff, Exploration of the active center structure of nitrogen-doped graphene-based catalysts for oxygen reduction reaction, *Energy Environ. Sci.* 5 (apr. 2012) 7936–7942, <https://doi.org/10.1039/C2EE21802J>.
- [4] X. Lu, Z. Li, X. Yin, S. Wang, Y. Liu, Y. Wang, Controllable synthesis of three-dimensional nitrogen-doped graphene as a high performance electrocatalyst for oxygen reduction reaction, *Int. J. Hydrogen Energy* 42 (27) (jul. 2017) 17504–17513, <https://doi.org/10.1016/j.ijhydene.2017.02.090>.
- [5] G. Lemes, D. Sebastián, E. Pastor, M.J. Lázaro, N-doped graphene catalysts with high nitrogen concentration for the oxygen reduction reaction, *J. Power Sources* 438 (oct. 2019), 227036, <https://doi.org/10.1016/j.jpowsour.2019.227036>.
- [6] H. He, Q. Yang, S. Xiao, X. Han, Q. Li, K. Lv, J. Hong, D. Tang, D. Kejian, Investigation of edge-selectively nitrogen-doped metal free graphene for oxygen reduction reaction, *J. Adv. Nanotechnol.* 1 (2) (2020) 5–13, <https://doi.org/10.14302/issn.2689-2855.jan-19-2744>, ene.
- [7] V.O. Mittal, H.R. Kunz, J.M. Fenton, Membrane degradation mechanisms in PEMFCs, *J. Electrochem. Soc.* 154 (7) (2007) B652, <https://doi.org/10.1149/1.2734869>.
- [8] S. Kawai, S. Saito, S. Osumi, S. Yamaguchi, A.S. Foster, P. Spijker, E. Meyer, Atomically controlled substitutional boron-doping of graphene nanoribbons, *Nat. Commun.* 6 (1) (2015), <https://doi.org/10.1038/ncomms9098>. Art. n.º 1, ago.
- [9] S. Yang, L. Zhi, K. Tang, X. Feng, J. Maier, K. Müllen, Efficient synthesis of heteroatom (N or S)-Doped graphene based on ultrathin graphene oxide-porous silica sheets for oxygen reduction reactions, *Adv. Funct. Mater.* 22 (17) (2012) 3634–3640, <https://doi.org/10.1002/adfm.201200186>.
- [10] Z.-S. Wu, W. Ren, L. Xu, F. Li, H.-M. Cheng, Doped graphene sheets as anode materials with superhigh rate and large capacity for lithium ion batteries, *ACS Nano* 5 (7) (2011) 5463–5471, <https://doi.org/10.1021/nn2006249>, jul.
- [11] M. Del Cueto, P. Ocón, J.M.L. Poyato, Comparative study of oxygen reduction reaction mechanism on nitrogen-, phosphorus-, and boron-doped graphene

- surfaces for fuel cell applications, *J. Phys. Chem. C* 119 (4) (2015) 2004–2009, <https://doi.org/10.1021/jp512588r>, ene.
- [12] F. Aguilar-Galindo, P. Ocoń, J.M.L. Poyato, Exploring the catalytic efficiency of X-doped (X=B, N, P) graphene in oxygen reduction reaction: influence of solvent and border effects, *Int. J. Quant. Chem.* 118 (14) (2018), e25579, <https://doi.org/10.1002/qua.25579>.
- [13] L. Dai, Y. Xue, L. Qu, H.-J. Choi, J.-B. Baek, Metal-free catalysts for oxygen reduction reaction, *Chem. Rev.* 115 (11) (jun. 2015) 4823–4892, <https://doi.org/10.1021/cr5003563>.
- [14] Z. Zhao, Z. Xia, Design principles for dual-element-doped carbon nanomaterials as efficient bifunctional catalysts for oxygen reduction and evolution reactions, *ACS Catal.* 6 (3) (mar. 2016) 1553–1558, <https://doi.org/10.1021/acscatal.5b02731>.
- [15] J. Liang, Y. Jiao, M. Jaroniec, S.Z. Qiao, Sulfur and nitrogen dual-doped mesoporous graphene electrocatalyst for oxygen reduction with synergistically enhanced performance, *Angew. Chem. Int. Ed.* 51 (46) (2012) 11496–11500, <https://doi.org/10.1002/anie.201206720>.
- [16] D.W. Stephan, Frustrated Lewis pairs: from concept to catalysis, *Acc. Chem. Res.* 48 (2) (2015) 306–316, <https://doi.org/10.1021/ar500375j>, feb.
- [17] D.W. Stephan, Frustrated Lewis pairs, *J. Am. Chem. Soc.* 137 (32) (2015) 10018–10032, <https://doi.org/10.1021/jacs.5b06794>, ago.
- [18] G. Skara, B. Pinter, J. Top, P. Geerlings, F. De Proft, F. De Vleeschouwer, Conceptual quantum chemical analysis of bonding and noncovalent interactions in the formation of frustrated Lewis pairs, *Chem. Eur. J.* 21 (march 2015) 5510–5519, <https://doi.org/10.1002/chem.201405891>.
- [19] L.M. Rivera, S. Fajardo, M.D.C. Arévalo, G. García, E. Pastor, S- and N-doped graphene nanomaterials for the oxygen reduction reaction, *Catalysts* 7 (9) (sep. 2017), <https://doi.org/10.3390/catal7090278>, Art. n.o 9.
- [20] M.J. Frisch, et al., «Gaussian 16 Rev. C.01», Wallingford, CT, 2016.
- [21] GaussView, Version 6, Dennington, Roy; Keith, Todd A.; Millam, John M. Semichem Inc., Shawnee Mission, KS, 2016.
- [22] Chemcraft, Graphical software for visualization of quantum chemistry computations, Version 1.8, build 648, <https://www.chemcraftprog.com>.
- [23] E.F. Pettersen, T.D. Goddard, C.C. Huang, G.S. Couch, D.M. Greenblatt, E.C. Meng, T.E. Ferrin, UCSF Chimera—a visualization system for exploratory research and analysis, *J. Comput. Chem.* 25 (13) (2004) 1605–1612, <https://doi.org/10.1002/jcc.20084>.
- [24] P. Hohenberg, W. Kohn, Inhomogeneous electron gas, *Phys. Rev.* 136 (3B) (1964) B864–B871, <https://doi.org/10.1103/PhysRev.136.B864>, nov.
- [25] C. Lee, W. Yang, R.G. Parr, Development of the Colle-Salvetti correlation-energy formula into a functional of the electron density, *Phys. Rev. B* 37 (2) (1988) 785–789, <https://doi.org/10.1103/PhysRevB.37.785>, ene.
- [26] S. Grimme, Semiempirical GGA-type density functional constructed with a long-range dispersion correction, *J. Comput. Chem.* 27 (15) (2006) 1787–1799, <https://doi.org/10.1002/jcc.20495>.
- [27] A.D. Becke, Density-functional thermochemistry. III. The role of exact exchange, *J. Chem. Phys.* 98 (7) (1993) 5648–5652, <https://doi.org/10.1063/1.464913>, abr.
- [28] R. Abouaf, S. Díaz-Tendero, Electron energy loss spectroscopy and anion formation in gas phase coronene, *Phys. Chem. Chem. Phys.* 11 (27) (jun. 2009) 5686–5694, <https://doi.org/10.1039/B904614C>.
- [29] H. Zettergren, G. Sánchez, S. Díaz-Tendero, M. Alcamí, F. Martín, Theoretical study of the stability of multiply charged C70 fullerenes, *J. Chem. Phys.* 127 (10) (sep. 2007), 104308, <https://doi.org/10.1063/1.2768361>.
- [30] F. Aguilar-Galindo, S. Díaz-Tendero, Theoretical insights into vinyl derivatives adsorption on a Cu(100) surface, *J. Phys. Chem. C* 122 (48) (2018) 27301–27313, <https://doi.org/10.1021/acs.jpcc.8b06142>.
- [31] T. Lu, F. Chen, Atomic dipole moment corrected hirshfeld population method, *J. Theor. Comput. Chem.* 11 (feb. 2012) 163–183, <https://doi.org/10.1142/S0219633612500113>, 01.
- [32] E.R. Johnson, S. Keinan, P. Mori-Sánchez, J. Contreras-García, A.J. Cohen, W. Yang, Revealing noncovalent interactions, *J. Am. Chem. Soc.* 132 (18) (may 2010) 6498–6506, <https://doi.org/10.1021/ja100936w>.
- [33] T. Lu, F. Chen, Multiwfn: a multifunctional wavefunction analyzer, *J. Comput. Chem.* 33 (5) (2012) 580–592, <https://doi.org/10.1002/jcc.22885>.
- [34] S. Miertuš, E. Scrocco, J. Tomasi, Electrostatic interaction of a solute with a continuum. A direct utilization of AB initio molecular potentials for the prevision of solvent effects, *Chem. Phys.* 55 (1) (feb. 1981) 117–129, [https://doi.org/10.1016/0301-0104\(81\)85090-2](https://doi.org/10.1016/0301-0104(81)85090-2).
- [35] S. Fajardo, P. Ocoń, J.L. Rodríguez, E. Pastor, Co supported on N and S dual-doped reduced graphene oxide as highly active oxygen-reduction catalyst for direct ethanol fuel cells, *Chem. Eng. J.* 461 (2023), 142053, <https://doi.org/10.1016/j.cej.2023.142053> abr.
- [36] R. Sibirian, H. Sihotang, S.L. Raja, M. Supeno, C. Simanjuntak, New route to synthesize of graphene nano sheets, *Orient. J. Chem.* 34 (1) (feb. 2018) 182–187, <https://doi.org/10.13005/ojc/340120>.
- [37] D.R. Dreyer, S. Park, C.W. Bielawski, R.S. Ruoff, The chemistry of graphene oxide, *Chem. Soc. Rev.* 39 (1) (2009) 228–240, <https://doi.org/10.1039/B917103G>, dic.
- [38] J. Li, Y. Zhang, X. Zhang, J. Huang, J. Han, Z. Zhang, X. Han, P. Xu, B. Song, S. N dual-doped graphene-like carbon nanosheets as efficient oxygen reduction reaction electrocatalysts, *ACS Appl. Mater. Interfaces* 9 (1) (2017) 398–405, <https://doi.org/10.1021/acsaami.6b12547>, ene.
- [39] J.-M. You, M.S. Ahmed, H.S. Han, J. eun Choe, Z. Üstündağ, S. Jeon, New approach of nitrogen and sulfur-doped graphene synthesis using dipyrrolemethane and their electrocatalytic activity for oxygen reduction in alkaline media, *J. Power Sources* 275 (feb. 2015) 73–79, <https://doi.org/10.1016/j.jpowsour.2014.10.174>.
- [40] S. Bag, B. Mondal, A.K. Das, C.R. Raj, Nitrogen and sulfur dual-doped reduced graphene oxide: synergistic effect of dopants towards oxygen reduction reaction, *Electrochim. Acta* 163 (may 2015) 16–23, <https://doi.org/10.1016/j.electacta.2015.02.130>.
- [41] H. Zhang, Y. Niu, W. Hu, Nitrogen/sulfur-doping of graphene with cysteine as a heteroatom source for oxygen reduction electrocatalysis, *J. Colloid Interface Sci.* 505 (2017) 32–37, <https://doi.org/10.1016/j.jcis.2017.05.069>, nov.
- [42] M. Klingele, C. Pham, K. Rao Vuyyuru, B. Britton, S. Holdcroft, A. Fischer, S. Thiele, Sulfur doped reduced graphene oxide as metal-free catalyst for the oxygen reduction reaction in anion and proton exchange fuel cells, *Electrochim. Commun.* 77 (2017) 71–75, <https://doi.org/10.1016/j.elecom.2017.02.015>, abr.
- [43] W. Yan, X. Cao, J. Tian, C. Jin, K. Ke, R. Yang, Nitrogen/sulfur dual-doped 3D reduced graphene oxide networks-supported CoFe₂O₄ with enhanced electrocatalytic activities for oxygen reduction and evolution reactions, *Carbon* 99 (2016) 195–202, <https://doi.org/10.1016/j.carbon.2015.12.011>, abr.
- [44] K. Kakaei, M.D. Esrafilii, A. Ehsani, *Oxyg. Reduct. React.* 27 (2019), <https://doi.org/10.1016/B978-0-12-814523-4.00006-X>.
- [45] C.F. Zinola, A.H. Castro Luna, W.E. Triaca, A.J. Arvia, Electroreduction of molecular oxygen on preferentially oriented platinum electrodes in acid solution, *J. Appl. Electrochem.* 24 (2) (feb. 1994) 119–125, <https://doi.org/10.1007/BF00247782>.
- [46] G. Pérez, E. Pastor, C.F. Zinola, A novel Pt/Cr/Ru/C cathode catalyst for direct methanol fuel cells (DMFC) with simultaneous methanol tolerance and oxygen promotion, *Int. J. Hydrogen Energy* 34 (23) (2009) 9523–9530, <https://doi.org/10.1016/j.ijhydene.2009.09.088>, dic.
- [47] G. Lemes, D. Sebastián, E. Pastor, M.J. Lázaro, N-doped graphene catalysts with high nitrogen concentration for the oxygen reduction reaction, *J. Power Sources* 438 (2019), <https://doi.org/10.1016/j.jpowsour.2019.227036>, September.
- [48] H. Bin Yang, C. Guo, L. Zhang, F. Xin Hu, W. Cai, J. Gao, C. Ming Li, B. Liu Yang, Nitrogen and sulfur Co-doped graphene inlaid with cobalt clusters for efficient oxygen reduction reaction, *Mater. Today Energy* 10 (2018) 184–190, <https://doi.org/10.1016/j.mtener.2018.09.011>.
- [49] J. Song, T. Liu, S. Ali, B. Li, D. Su, The synergy effect and reaction pathway in the oxygen reduction reaction on the sulfur and nitrogen dual doped graphene catalyst, *Chem. Phys. Lett.* 677 (jun. 2017) 65–69, <https://doi.org/10.1016/j.cplett.2017.03.088>.
- [50] M. Keramatnia, B. Ramezanzadeh, M. Mahdavian, G. Bahlakeh, Chemically controlled nitrogen-doped reduced-Graphene/Graphite oxide frameworks for aiding superior thermal/anti-corrosion performance: integrated DFT-D & experimental evaluations, *Chem. Eng. J.* 437 (2022), 135241, <https://doi.org/10.1016/j.cej.2022.135241> jun.
- [51] H.W. Kim, V.J. Bukas, H. Park, S. Park, K.M. Diederichsen, J. Lim, Y.H. Cho, J. Kim, W. Kim, T.H. Han, J. Voss, A.C. Luntz, B.D. McCloskey, Mechanisms of two-electron and four-electron electrochemical oxygen reduction reactions at nitrogen-doped reduced graphene oxide, *ACS Catal.* 10 (1) (2020) 852–863, <https://doi.org/10.1021/acscatal.9b04106>, ene.